Magnetic Field Projection and Current Phase Control in a 2-D Planar Transmitting Coil Array

Ning Kang , *Member, IEEE*, Haojun Qin , *Graduate Student Member, IEEE*,
Ruihan Ma , *Graduate Student Member, IEEE*, Christopher H. T. Lee , *Senior Member, IEEE*,
Ming Liu , *Senior Member, IEEE*, and Chengbin Ma , *Senior Member, IEEE*

Abstract—**Wireless power transfer systems operating at frequencies of several megahertz are of interest due to their high spatial freedom and compactness. Combining multiple transmitting (Tx) coils for magnetic field shaping has emerged as a promising candidate to further improve the spatial freedom of the power transfer. In this article, a new closed-loop-based scheme is developed for detecting the spatial position / orientation of multiple receivers (Rxs) and controlling the magnetic field distribution accordingly. Inspired by the orthogonal projection of visible light, this article proposes the concept of magnetic field projection to detect the position and orientation of multiple Rxs. Using a 2×2 Tx-coil array as an example, a coding-based detection approach is developed using the results of the magnetic field projections in the x, y, and z directions. A control flow is then proposed for determining the optimal phase combination of the power amplifier (PA) output currents to achieve the desired magnetic field shaping. Finally, the above concepts are experimentally realized and verified. Light-emitting-diode arrays were specially fabricated to visualize the actual magnetic field shaping results. It is found that the final system can accomplish the closed-loop detection of the three spatially distributed Rxs and the phase control of the PA output current within 25 ms. This article is accompanied by two video files to demonstrate the actual detection and control process.**

Index Terms—**Magnetic field shaping, megahertz, phase-shift control, position and orientation detection, transmitting coil array, wireless power transfer (WPT).**

I. INTRODUCTION

WIRELESS power transfer (WPT) has attracted considerable attention thanks to its convenient, flexible, and

safe supply of power. Currently, most commercial WPT systems operate in the kilohertz (kHz) bands [1], [2]. Many efforts have been made to improve the performance of kHz WPT systems through innovations in circuit topology, coil design, and control [3], [4], [5], [6]. At the same time, increasing the operating frequency to the megahertz (MHz) bands is beneficial to the degree of spatial freedom and the compactness of final systems [7], [8], [9]. Concurrently, ever-increasing requirements on the high degree of spatial freedom remain to be an ongoing challenge for both kHz WPT and MHz WPT, especially when there are multiple receivers with different positions and orientations. Approaches (such as through repeaters, coil designs, and matching networks) have been proposed to further improve the important spatial freedom [10], [11], [12], [13]. However, the magnetic field distribution of conventional WPT systems is generally considered to be uncontrollable. For instance, various single 3-D transmitting (Tx) coils have been used to generate a fixed omnidirectional magnetic field distribution [14], [15]. A specially designed 3-D receiving (Rx) coil was also developed to reduce output power variation when the Rx position or orientation changes [16], [17]. In addition, direct quadrature Tx or Rx coils with ferrite cores have been proposed for wide-range omnidirectional power transfer [18], [19], [20]. Various 2-D Tx-coil designs have also been applied to generate a rotating uniform magnetic field [21], [22].

So-called magnetic field shaping can control the B-field distribution through applying different currents in multiple Tx coils. It has emerged as a promising candidate to further enhance the performance of today's WPT systems, such as in transfer distance, efficiency, and power capability. Rx detection and B-field control are central to an effective magnetic field shaping. Therefore, considerable attention has been paid to this detection and control aspect based on 3-D Tx-coil designs, and most of those existing works operated in the kHz bands [23], [24], [25], [26], [27], [28], [29]. For instance, a spherically shaped 3-D Tx-coil structure was proposed to achieve the magnetic field shaping through the amplitude control of the Tx output currents [23]. The final system operated at 535 kHz and performed the Rx detection through scanning all the 200 directions. With a different cubic-shaped structure using three orthogonal Tx coils, a 3-D gradient descent method was introduced to optimize the Tx-coil current magnitudes, and thus charge multiple moving receivers with a 20 kHz operating frequency and a 200 ms convergence time [24]; an extremum-seeking algorithm was

TABLE I
LIGHT PROJECTION VERSUS MAGNETIC FIELD PROJECTION

Forest green: Light source versus Tx coils; Bright green: (Active) Light versus Magnetic flux; Red: Object versus Rx coil; Dark green: Shadow versus PA input currents; Gray contour: (Inactive) Light versus Magnetic flux.

also applied to achieve the maximum power transfer to a single dynamic Rx in 150 ms [25]. A current amplitude control scheme was developed for a bowl-shaped omnidirectional 6.78 MHz WPT system to detect the multi-Rx orientations and focus the power flow towards each receiver [28]. Every five minutes, a step-by-step detection algorithm was applied to identify the positions and orientations of multiple Rxs, and a maximum point tracking function further improves the system efficiency.

Meanwhile, 2-D planar Tx coils have recently received significant interest for the magnetic field shaping thanks to their compactness and increased design freedom of the Tx coils (number, layout, and shape, etc.) [30], [31], [32], [33]. Based on classic magnetic field vector analysis in the 3-D Tx coils, an excitation current vector modulation strategy via communication between the Tx and Rx was designed to achieve arbitrary angular misalignment of a single Rx [30]. An automatic tuning algorithm was developed via an exhaustive phase sweep that resulted in the highest rectified voltage [31]. A 2-D Tx-coil array was proposed to power multiple Rxs with six degrees of spatial freedom [32]. It especially provides extendability via effective cross coupling minimization. Constant output power of a single Rx can be further realized when applying a 2-D Tx-coil array, in which a camera-based visual detection of the Rx position and orientation is proposed [33]. In most existing literature, each Tx coil is controlled to generate its own magnetic field vector in a fixed direction, x, y, or z-direction. This fixed direction limits the flexibility in the magnetic field shaping and design of a specific Tx-coil array layout. There is a lack of a comprehensive detection and control scheme that makes the best use of the nature of a 2-D planar Tx-coil array.

Unlike existing 3-D Tx coils, the coils in a 2-D Tx-coil array are not perpendicular to each other. Therefore, the assumption that the magnetic field vector is perpendicular to its coil plane

no longer holds. Conversely, the proposed 2-D Tx-coil array allows each Tx coil to dynamically generate multidirectional magnetic field vectors through precise phase control of the coil currents. This capability greatly enhances the flexibility of magnetic field shaping. In particular, the proposed 2-D planar Tx-coil array is demonstrated to have the capability to generate a transverse magnetic field via proper phase control of the Tx-coil currents. By making full use of this unique advantage (i.e., easiness to generate transverse magnetic field), this article develops a new closed-loop-based scheme to detect spatial positions / orientations of multiple receivers and control the magnetic field distribution accordingly. Combined with an MHz operating frequency, the spatial freedom of power transfer and the compactness of final systems can be further improved. The proposed control scheme is general to address a 2-D planar Tx-coil array with a different number of Tx and Rx coils. For a WPT system with a random number of Rxs, the position and orientation of each Rx can be determined by three times magnetic field projections in x, y, and z directions, respectively, achieved with three different combinations of the Tx-coil current phases. The proposed detection only needs to measure the input dc currents of the Tx coils, without requiring communication between Tx side and Rx side. Thanks to the developed simple and efficient scheme, the final experimental system can complete the closed-loop phase control within 25 ms, even with three Rxs in six degrees of spatial freedom.

The rest of this article is organized as follows. Section II presents the basic idea of the magnetic field projection for multi-Rx position and orientation detection based on the orthogonal projection of visible light [see Table I]. Taking a 2×2 Tx-coil array as an example, Section III introduces the principle of the Rx detection. It first delineates all the possible spatial locations and orientations of the Rxs. Then, a detailed magnetic flux

analysis is performed for the cases of single Rx and multiple Rxs. Section IV describes a complete detection and control algorithm including state monitoring and power amplifier (PA) output current phase shift control. Then, in Section V, the proposed detection and control scheme is validated by comprehensive experiments. Section VI further discusses practical aspects. Finally, Section VII concludes this article.

II. PRINCIPLE OF ORTHOGRAPHIC PROJECTION

Detecting the position and orientation of single or multiple Rxs is the key to achieving an effective 3-D magnetic field shaping to maximize power transfer capability and efficiency. However, implementing multiple-Rx position and orientation detection is challenging because each Rx has six independent degrees of spatial freedom. Taking a WPT system with three Rxs as an example, the Rxs have eighteen degrees of spatial freedom (DOF) in total, and in each DOF, there are numerous possibilities. This makes traditional solutions (e.g., conventional look-up table-based algorithms) infeasible. In addition, as described in Section I, current literature lacks a solution to detect the Rx positions and orientations without communication between the transmitter and receiver.

This article introduces the principle of orthogonal projection as a novel solution to detect the six-DOF positions and orientations of Rxs. As shown in Table I, it is intuitive that the projected graphics in the x, y, and z directions indicate the 3-D shape and position of an object. If visible light is replaced with the magnetic flux, the opaque objects are actually equivalent to the Rxs. Therefore, this orthographic projection solution can also be extended to detect the Rx position and orientation for the present 3-D magnetic field shaping problem, such as through an extendable planar Tx-coil array.

Inspired by the light projection in Table I, if the Tx-coil array can separately generate magnetic fields in x, y, and z directions, the Rx can also be effectively "projected" in the three directions. By applying different current phases (such as $0°$ and $180°$) in the rows or columns of the coil array, the magnetic field can be formed mainly towards x or y or z direction. Other phase combinations can also be used to generate magnetic field in different directions for Rx detection purposes. Meanwhile, as same as the nonorthogonal projection, such combinations may complicate the analysis of magnetic field projection results. Note that from a strictly physical perspective, all magnetic lines are closed with no start or end points. However, the lower figures in Table I illustrate only a portion of these lines for clarity.

Therefore, a step-by-step process of the three times (x or y or z direction) of magnetic projection can be as follows.

1) First, the magnetic flux in x-direction is generated by applying a corresponding combination of current phases to individual coils in the planar Tx-coil array.
2) Then, the input dc power (or current given a specific PA input voltage) of all the PAs is measured and recorded. This is because the input dc power of a specific PA is positively correlated with the amount of magnetic flux (generated by the Tx coil that the PA drives) passing through single or multiple Rx coils, namely a "projection" of magnetic

flux. This avoids direct magnetic flux measurements that require additional sensors and equipment.
3) Similarly, the magnetic flux in y- and z-direction is generated sequentially, and again their corresponding PA input dc power is respectively measured and recorded.
4) Finally, based on the combination of all the above measured PA input dc power, the Rx positions and orientations can be determined, as detailed in the following Section III.

III. DETECTION OF RECEIVERS

For ease of discussion, a 2×2 Tx-coil array in Table I is taken as an example. Through different combinations of current phases, the magnetic field projections in x, y, and z directions can be generated. Note that for clarity of illustration, the Tx coils in the schematic diagram are shown without overlap, unlike those in the following experiments. Increasing the number of coils in the Tx-coil array certainly improves the directionality of the magnetic field. Meanwhile, as verified in the following sections, the proposed Rx detection still works well for the example 2×2 Tx-coil array here.
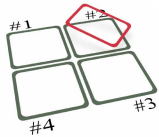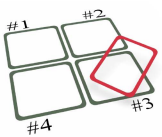
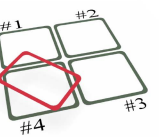### A. Categories of Rx Positions and Orientations
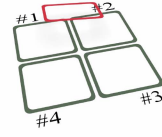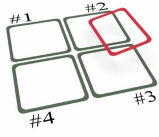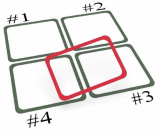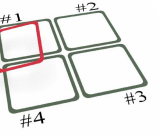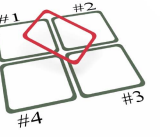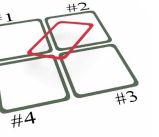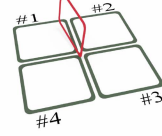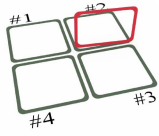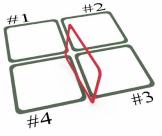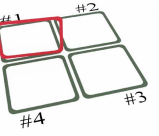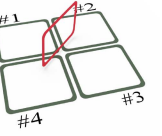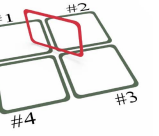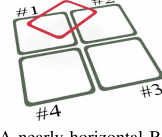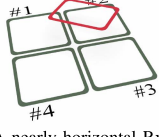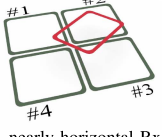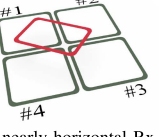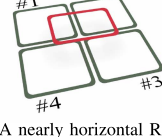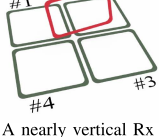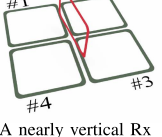
All possible Rx positions and orientations for the 2×2 Tx-coil array are listed in Table II. They are categorized based on two types of information or criteria: 1) the serial number(s) of the Tx coil(s) powering the Rx; and 2) a rough classification of the Rx's orientation (nearly horizontal or nearly vertical). Both of them can be indicated by observing the PA input dc currents under the magnetic field projections in different x, y, and z directions. Note that due to the geometric symmetry of the present Tx-coil array, in the current setup, only an even number (i.e., one or two pairs) of Tx coils can generate horizontal flux that effectively passes through a nearly vertical Rx coil. Therefore, in Table II, all eight nearly vertical Rx cases fall into categories II and IV, where the Rx is simultaneously powered by an even number of Tx coils (two or four Tx coils). In addition, a reasonable assumption in the following analysis is that the size of an Rx is similar to the size of an individual Tx coil. Thanks to the 2-D distributed Tx-coil array, it is usually easy to adjust the Tx-coil size for a specific application.

B. Single Rx Detection

A general principle is as follows.
1) *Position of Rx:* For an Rx with a fixed position and orientation, the power received from each individual Tx coil can be different. For instance, when Rx is near a corner of the 2×2 Tx-coil array, only one specific Tx coil and the Rx have strong coupling, which can be indicated by the corresponding PA input dc current. For example, since many consumer electronic devices (e.g., cellphones) have a minimum input power of 5V-1 A, it is reasonable to assume that the minimum Rx power received is 5 W. Assuming a system dc–dc efficiency of about 75% in low-power mode, the nearest Tx coil should have an input power of at least 6.7 W. Given a specific PA input voltage,

TABLE II
FOUR CATEGORIES OF RX POSITIONS AND ORIENTATIONS
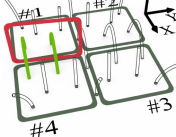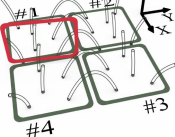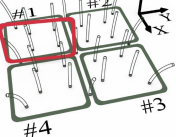
Categories	Scenes
I	An Rx above Tx#1 An Rx above Tx#2 An Rx above Tx#3 An Rx above Tx#4
II	A nearly horizontal Rx above Tx#1,2 A nearly horizontal Rx above Tx#2,3 A nearly horizontal Rx above Tx#3,4 A nearly horizontal Rx above Tx#4,1 A nearly horizontal Rx above Tx#1,3 A nearly horizontal Rx above Tx#2,4 A nearly vertical Rx above Tx#1,2 A nearly vertical Rx above Tx#2,3 A nearly vertical Rx above Tx#3,4 A nearly vertical Rx above Tx#4,1 A nearly vertical Rx above Tx#1,3 A nearly vertical Rx above Tx#2,4
III	A nearly horizontal Rx above Tx#4,1,2 A nearly horizontal Rx above Tx#1,2,3 A nearly horizontal Rx above Tx#2,3,4 A nearly horizontal Rx above Tx#3,4,1
IV	A nearly horizontal Rx above Tx#1,2,3,4 A nearly vertical Rx above Tx#1,2,3,4 A nearly vertical Rx above Tx#1,4,2,3

the threshold of the PA input dc current can be determined accordingly, as described in Section V. Note that because of the use of the threshold, in the following case of multiple Rx detection, the actual power consumption of all the Rxs may not necessarily be the same, as is also validated in the final experiments.

2) *Orientation of Rx:* The possible Rx orientations can be classified as nearly horizontal and nearly vertical. As mentioned in Section II above, for a nearly horizontal Rx, Tx coils with the same current phase can effectively power it, i.e., the z-direction magnetic field projection; while for a nearly vertical Rx, Tx coils with a 180° current phase difference can power it, i.e., the x- or y-direction magnetic field projection [see Table I].

Based on the above basic considerations, Table III shows an example of the magnetic field projections of a single Rx, in which the Rx is nearly vertical and interacts mainly with the two nearest Tx coils, #1 and #4. In Table III, the gray lines represent the magnetic flux that does not pass through the Rx coil, while the green lines are the magnetic flux powering the Rx. Here, 1 and 0 are assigned to each Tx coil to indicate whether
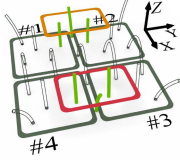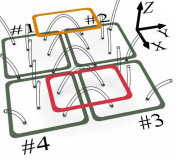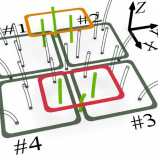
TABLE III
EXAMPLE OF SINGLE-RX DETECTION*

Projections	x-direction Projection (0°, 0°, 180°, 180°)				y-direction Projection (0°, 180°, 180°, 0°)				z-direction Projection (0°, 0°, 0°, 0°)			
Tx-coil No.	1	2	3	4	1	2	3	4	1	2	3	4
Active (Y/N)	Y	N	N	Y	N	N	N	N	N	N	N	N
Calculated Codeword	1	0	0	1	0	0	0	0	0	0	0	0
Red-Rx Codeword	1	0	0	1	0	0	0	0	0	0	0	0

* A nearly vertical Red-Rx above Tx#4,1.

this Tx-coil powers the Rx in a specific direction (x, y, or z) of the magnetic field projection. For the present example, the codes of the x, y, and z-direction projections are [1 0 0 1],

TABLE IV
EXAMPLE FOR TWO-RX DETECTION*

Projections	x-direction Projection (0°, 0°, 180°, 180°)				y-direction Projection (0°, 180°, 180°, 0°)				z-direction Projection (0°, 0°, 0°, 0°)			
Scenes												
Tx-coil No.	1	2	3	4	1	2	3	4	1	2	3	4
Active (Y/N)	Y	Y	Y	Y	N	N	N	N	Y	Y	Y	Y
Calculated Codeword	1	1	1	1	0	0	0	0	1	1	1	1
Red-Rx Codeword	0	0	1	1	0	0	0	0	0	0	1	1
Yellow-Rx Codeword	1	1	0	0	0	0	0	0	1	1	0	0

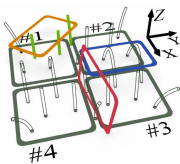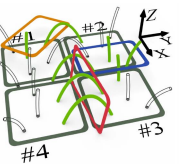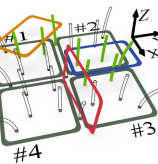* A nearly horizontal Red-Rx above Tx#3,4 and
a nearly horizontal Yellow-Rx above Tx#1,2.

TABLE V
EXAMPLE FOR THREE-RX DETECTION*

Projections	x-direction Projection (0°, 0°, 180°, 180°)				y-direction Projection (0°, 180°, 180°, 0°)				z-direction Projection (0°, 0°, 0°, 0°)			
Scenes												
Tx-coil No.	1	2	3	4	1	2	3	4	1	2	3	4
Active (Y/N)	Y	N	N	N	Y	Y	Y	Y	Y	Y	Y	N
Calculated Codeword	1	0	0	0	1	1	1	1	1	1	1	0
Red-Rx Codeword	0	0	0	0	0	0	1	1	0	0	0	0
Yellow-Rx Codeword	1	0	0	0	1	0	0	0	1	0	0	0
Blue-Rx Codeword	0	0	0	0	0	1	1	0	0	1	1	0

* A nearly vertical Red-Rx above Tx#3,4, a Yellow-Rx above Tx#1,
and a nearly horizontal Blue-Rx above Tx#2,3.

Fig. 1. Detection of six-Rx positions and orientations via a 4×4 planar Tx-coil array.

Refer to Table II:
Category I: ①
Category II: ② ④
Category III: ⑥
Category IV: ③ ⑤

Rx Serial Number

TABLE VI
PHASE COMBINATIONS IN MAGNETIC FIELD PROJECTIONS*

Arrays	x-direction Projection	y-direction Projection	z-direction Projection
2 × 3			
4 × 4			
Arbitrary dimension			

* Black coils: In-phase currents (0°);
Green coils: Out-of-phase currents (180°).

[0 0 0 0], and [0 0 0 0], respectively [see Table III]. Note that this sensing capability is a unique advantage of applying the 2-D planar Tx-coil arrays. Unlike conventional single Tx-coil solutions, the Tx-coil arrays discussed here can both provide sensing and power transfer capabilities. As shown in Table II, all the possible positions and orientations of a single Rx have their own unique combinations of the four-bit codes in x, y, and z-direction magnetic field projections. Theoretically, this detection approach has 12-bit resolution.

C. Multiple Rx Detection

The above magnetic field projection-based single-Rx detection method can be further extended to address the cases with multiple Rxs. Tables IV and V show two examples of two-Rx and three-Rx detection, respectively. The detection can be based on the above procedures developed for a single Rx and the superposition principle. It is because a relatively small number of Rxs (such as 1–3 Rxs in the current case) do not significantly affect the distribution of the magnetic field. For instance, in Table IV, assuming that there is only a red Rx coil, then the binary codes for the x, y, and z-direction magnetic field projects are [1 1 0 0], [0 0 0 0], and [1 1 0 0]. For a yellow Rx coil, the codes are [0 0 1 1], [0 0 0 0], and [0 0 1 1]. Consequently, the final codes for the present two-Rx position and orientation detection are [1 1 1 1], [0 0 0 0], and [1 1 1 1]. This combination forms a 12-bit code that does not belong to any known code for a single Rx detection. A similar principle can be applied to a three-Rx case, as shown in Table V.

Fig. 1 shows that it is possible to detect positions and orientations of six Rxs via a 4×4 Tx-coil array following the same set of categories in Table II. Table VI further shows that the above detection principle is applicable to Tx arrays with arbitrary 2-D dimensions. It should be noted that the detection resolution is largely decided by the number of coils in the planar Tx-coil
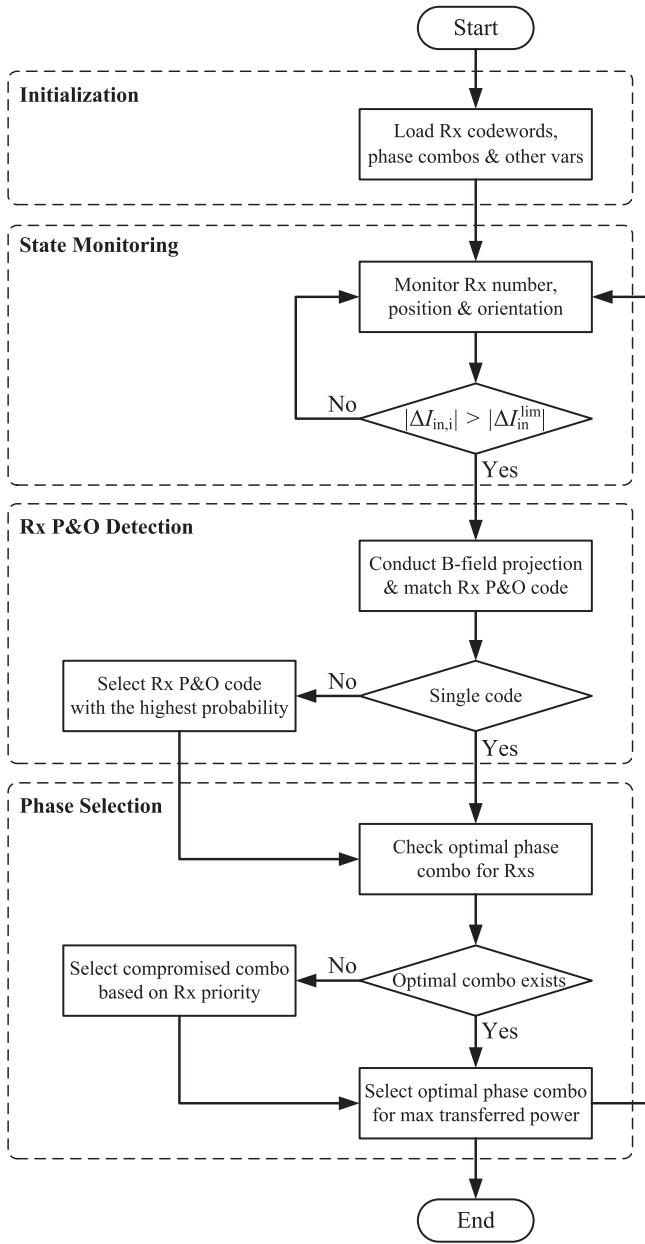
Fig. 2. Flowchart of the closed-loop phase control of PA output currents.

array and relative sizes of the Rx coils. If necessary, additional levels of PA dc input currents beyond the two binary levels can be defined to further enhance the resolution of Rx position and orientation detection.

IV. PA OUTPUT CURRENT PHASE CONTROL

A. Control Flow

The flowchart in Fig. 2 summarizes the main procedures of PA output current phase control in a planar Tx-coil array. Based on the above Rx position and orientation detection, the purpose of this closed-loop control is to implement an optimal 3-D magnetic field shaping for a specific set of Rxs. It is important to first define several key PA related variables because the PA

input dc currents are the only required feedback signals for the detection.

1) $I_{\text{in},i}$: The dc input current of the ith PA detected within a certain sampling period.
2) $\Delta I_{\text{in},i}$: The variation in $I_{\text{in},i}$ compared to its last sampling.
3) $\Delta I_{\text{in}}^{\text{lim}}$: A threshold of $\Delta I_{\text{in},i}$ that indicates the change of Rx positions and orientations.

The PA output current phase control is conducted step-by-step as follows.

1) *Initialization:* A microcontroller (MCU) first loads all the prestored Rx position and orientation codes and their corresponding optimal combinations of PA output current phases, specific phase combinations for the x, y, z-direction magnetic field projections, and threshold of the PA dc input current variation $\Delta I_{\text{in}}^{\text{lim}}$. Note that the selection of the optimal phase combinations will be discussed in next subsection.
2) *State Monitoring:* The MCU monitors all the four PA input dc currents (i.e., each of the $I_{\text{in},i}$ values). It detects new changes in Rx number, positions, or orientations by constantly checking the value of $\Delta I_{\text{in},i}$. If any $\Delta I_{\text{in},i}$ is greater than $\Delta I_{\text{in}}^{\text{lim}}$, new changes in Rx number, positions, and orientations should happen and the MCU starts new magnetic field projections to update the Rx positions and orientations.
3) *Rx Position and Orientation (P&O) Detection:* The MCU controls the Tx-coil array to conduct the x, y, and z-direction magnetic field projections. Then, it converts a set of detected PA dc input currents into a binary code. Initially focusing on single Rx detection, as described in the above section, the MCU compares the binary code with all the prestored Rx position and orientation codes
   a) If the newly converted binary code exactly matches one of the prestored codes, the corresponding optimal PA output current phase combination will be applied.
   b) If the binary code does not match any prestored codes, the similarity (e.g., represented as the Hamming distance) between them will be compared to identify the most similar prestored code. The resulting detection of the Rx position and orientation will then be based on this prestored code. This decoding approach is commonly used in communication systems. Note that in multi-Rx cases, the above comparison process should be executed between the converted binary code and superpositions of prestored codes [see Tables IV and V].
4) *Phase Selection:* Based on the Rx position and orientation detection results, an optimal combination of the PA output current phases will be determined and discussed in the upcoming subsection.

B. Selection of Phase Combination

For a single receiver, a PA output current phase combination with maximized magnetic flux passing through the Rx can be considered to be optimal. The purpose of this combination is to maximize the receiving power. In such a case, the Rx draws the most power when the PA output currents in the Tx coils are

Number of active Tx coil (s)	Rx orientation	Optimal phase
One (category I)	–	Any phase
Two (category II)	Nearly-horizontal	In-phase
	Nearly- vertical	Out-of-phase
Three (category III)	Nearly-horizontal	In-phase
Four (category IV)	Nearly-horizontal	In-phase
	Nearly- vertical	Out-of-phase

* Refer to Table II for the four categories.

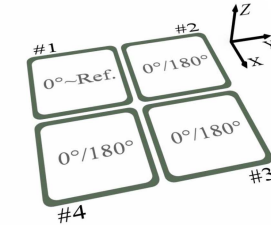Fig. 3. Selection of PA output current phase combination for a single Rx.

either in-phase or out-of-phase (i.e., $0°$ or $180°$), as summarized in Table VII [34], [35]. In the example 2×2 Tx-coil array, the typical phase combinations that may enable an Rx to receive the maximum power include eight combinations, assuming that the output current phase of Tx#1 is a reference phase, i.e., $0°$ [see Fig 3]. As mentioned above, the MCU prestores the correspondence between the detected Rx positions / orientations

(i.e., the converted binary codes) and optimal phase combinations, and implements a specific phase combination based on the latest detection result. For instance, Fig 3 shows an example case of a single nearly vertical Rx above and between Tx#4 and Tx#1. This specific Rx position and orientation, which belongs to the category II in Table VII, can be detected through the x, y, and z-direction magnetic field projections. Then, the corresponding out-of-phase solution of the Tx#4 and #1's PA output currents (i.e., $180°$ and $0°$, respectively) is determined. Meanwhile, Tx#2 and #3 remain inactive and have minimal impact on the Red-Rx. Therefore, the phases of these two Tx coils are arbitrary.

For multiple receivers, a final phase combination can be determined as follows.

1) Prestore the optimal phase combinations of each single Rx position and orientation in the MCU.
2) After obtaining the positions and orientations of all the Rxs, check whether a common phase combination exists that allows all the Rxs to receive maximum power simultaneously.
3) If there is no common phase combination, a compromised phase combination must be determined to power each Rx. Multiple strategies are possible for different purposes, such as prioritizing the Rx located at the edge to obtain enough power and ensuring that the other Rxs also receive sufficient power. This article adopts a strategy of prioritizing an Rx at the edge because there are fewer Tx coils available to power it.

To further explain, two examples are shown in Fig 4, in which "√" denotes an optimal phase combination for an individual Rx. In Fig. 4(a), the Rx positions and orientations are first detected through the magnetic field projections, indicating that the red, yellow and blue Rxs can be potentially powered by Tx#3,4, Tx#1, and Tx#2,3, respectively. Their optimal PA output current phase combinations can then be determined, and two common combinations are $[0°, 0°, 0°, 180°]$ and $[0°, 180°, 180°, 0°]$. The final magnetic flux distribution, taking the first combination as an example, shows that each Rx has the maximized magnetic flux passing through. For the second example, namely Fig. 4(b), the red and yellow Rxs can be mostly powered by Tx#1,2,3,4 and Tx#1,2, respectively, because of their different positions and orientations. There is no common optimal phase combination in this example. As mentioned above, a compromised strategy is to prioritize the power received by the yellow Rx at the edge, but make sure the red Rx also receives a sufficient amount of power. The final compromised phase combinations are $[0°, 0°, 0°, 180°]$ and $[0°, 0°, 180°, 0°]$, namely with reversed current phases in Tx#3 and 4. Again, the first combination is taken as an example and its magnetic flux distribution is shown in Fig. 4(b). Finally, the above principle of phase combination selection is general for more complex cases, such as the one shown in Fig. 1.

V. EXPERIMENTAL RESULTS

A. Circuit Configuration and Implementation

Fig. 5 shows the circuit configuration of an experimental 6.78 MHz WPT system, featuring an extendable planar Tx-coil array and multiple receivers. The transmitter utilizes multiple

Fig. 4. Selection of PA output current phase combination for multiple Rxs. (a) With common combinations. (b) Without common combinations.

current-mode Class E PAs operating at 6.78 MHz to individually drive their corresponding Tx coils, while a single receiver comprises its own Rx coil and a full-wave Class E rectifier. In each current-mode Class E PA, a T-matching network is added between the conventional Class E PA and transmitting coil [36]. Physically, there is only one additional parallel capacitor $C_{\mathrm{t,p}}$ because the other two elements, namely two inductors, are absorbed by $L_{0,\mathrm{p}}$ and $L_{\mathrm{tx,p}}$, respectively.
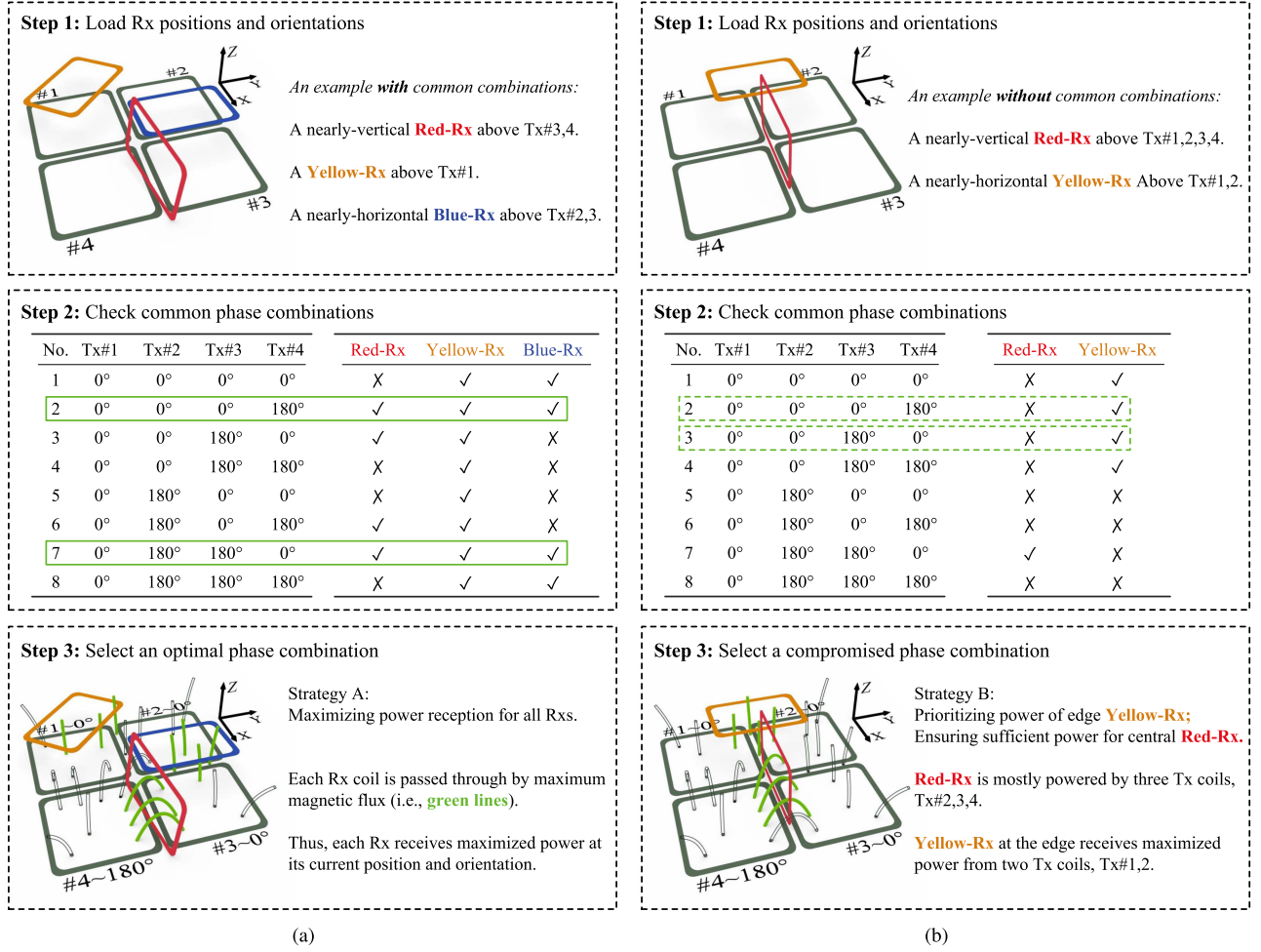
The final experimental WPT system is shown in Fig. 6, adopting the same configuration as depicted in Fig. 5. The four PA switches, Q_{1-4}, employ GaN transistors (GS61004B), while the capacitors are implemented by using Murata's multilayer ceramic capacitors with a tolerance of 5%. A minimal FPGA system board is used to generate a four-channel phase-shifted PA driving signal. To ensure maximum transferred power, here only 0° or 180° phase difference (i.e., in-phase or out-of-phase) is required [see Table VII]. Meanwhile, today's FPGA and dedicated phase delay ICs both support phase shift modulation with an accuracy up to 0.25 ns. This accuracy is sufficient to provide a higher phase difference resolution for the 6.78 MHz driving signal in order to adopt additional control strategies. The Tx- coil array, measuring 20 cm × 20 cm, consists of four

TABLE VIII
MEASUREMENT RESULTS OF TX-COIL CROSS-COUPLING COEFFICIENTS

Tx-coil pair	Tx#1,2	Tx#1,3	Tx#1,4	Tx#2,3	Tx#2,4	Tx#3,4
Coefficient	0.010	0.018	0.002	0.010	0.016	0.010

square coils. As shown in Table VIII, the average cross-coupling coefficient between these coils has been minimized to 0.011 by an important coil overlap design, as detailed in [32] and shown in Figs. 6 and 7, to suppress interference between the individual Tx coils and thus achieve stable operation of the PAs. There are three Rxs that may have different positions, orientations, and dc loads. For the sake of simplicity, the three Rx coils are with the same size (10 cm × 7 cm), approximately two-thirds the size of an ordinary cellphone.

As shown in Fig. 7, in real implementation, four current sensors monitor the four-channel PA dc input currents, and four active filters remove high-frequency noise from the sampled current signals. An MCU, specifically the STM32, processes the current signals and send them to the FPGA. Finally, through the parallel operation of the FPGA, the phase-shifted signals are
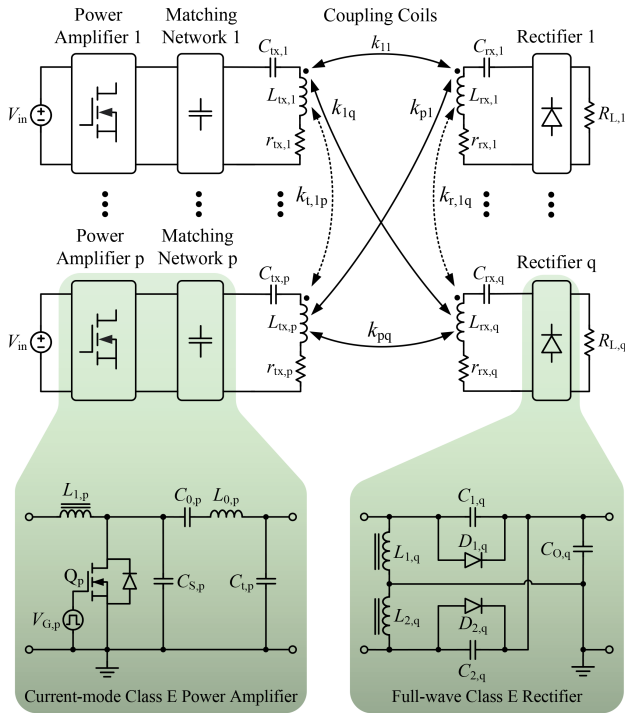
Fig. 5. Circuit configuration of a 6.78 MHz WPT system with an extendable planar Tx-coil array and multiple Rxs.
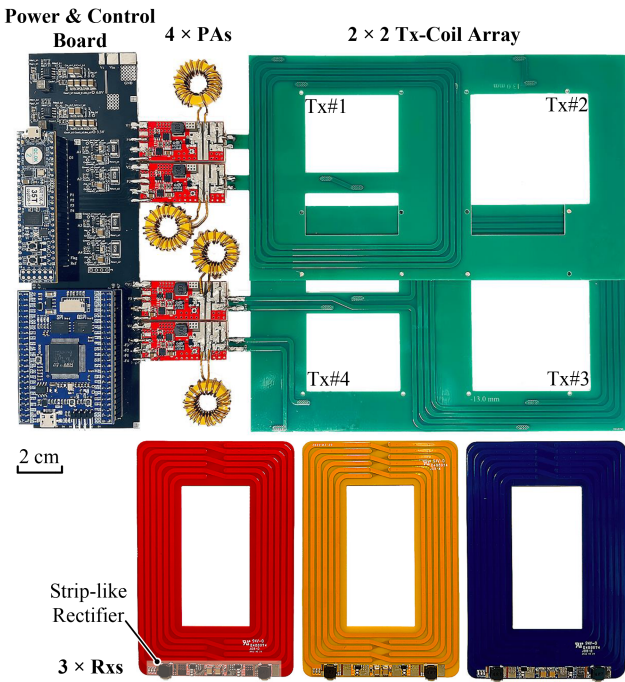

Fig. 6. Actual 6.78 MHz WPT system with closed-loop phase control.

output to the switches of the four PAs. In addition, the STM32 also sends real-time Rx position and orientation detection results to a host computer via Bluetooth communication. In particular, the three Rxs have different loads of 5 Ω, 10 Ω, and 20 Ω, respectively.
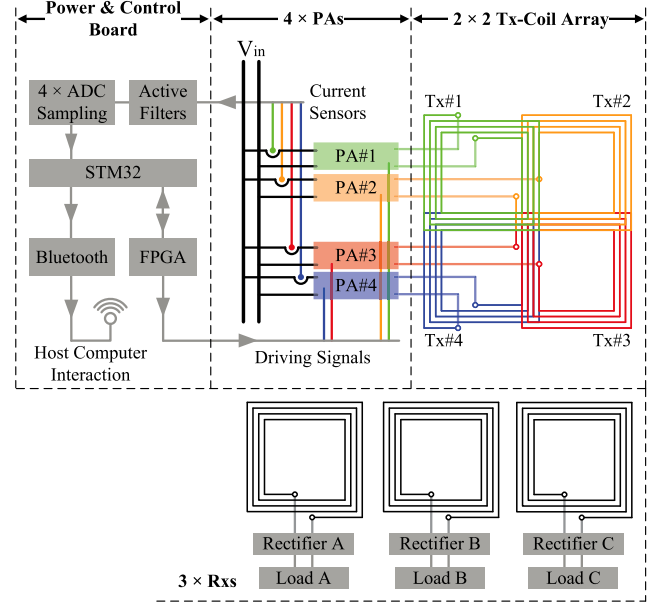

Fig. 7. Block diagram of real implementation.

B. Visualization of Magnetic Field Projections

As shown in Table IX, a 3-D structure with 41 LED receiving modules (2.0 cm × 2.0 cm each) is built up to visualize the magnetic field projections. A 2×4 blue vertical LED array indicates the x-direction B-field, while a 2×4 red vertical LED array indicates the y-direction B-field. A 5×5 green LED array covers an area of 20 cm × 20 cm to indicate the z-direction B-field. Note that the brightness of the LEDs has a nonlinear relationship with the B-field strength. The six figures in the table verify the theoretical analysis in Section II. For instance, for the x-direction projection, the red LEDs indicating the y-direction B-field are all OFF, while the blue LEDs are all ON. This result validates the theoretical result in the x-direction magnetic field projection. Furthermore, the experimental results in the y and z-direction projects also closely match their respective theoretical results.

C. Detection of Fixed Rx Positions and Orientations

Table X shows the results of the magnetic field projections for a single Rx. Note that circuits (PAs, rectifiers, etc.) are not shown in the photo for clarity. To meet the typical minimum input power of 5 W in consumer electronic devices, the minimum input power for the WPT system should be 6.7 W, as described in Section III. Consequently, in the experimental setup where the system's input voltage is 24 V, the PA dc input current threshold is set at 0.28 A, calculated from 6.7 W / 24 V, which determines the activation of a specific Tx coil. As shown in the table, based on the feedback of PA dc input currents and the above threshold, active Tx coils that power the Rx can be identified. These detection results are converted to three sets of four-bit binary codes, each corresponding to the x, y, and z-direction magnetic field projections. As discussed in Section III-B, a combination of the three four-bit codes corresponds to one specific Rx position and orientation, with all the theoretical and experimental codes in the x, y, and z-direction projections aligning identically.

TABLE IX
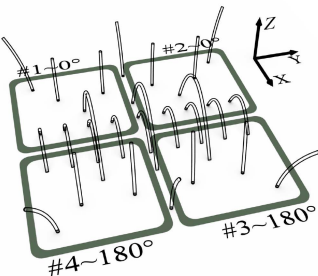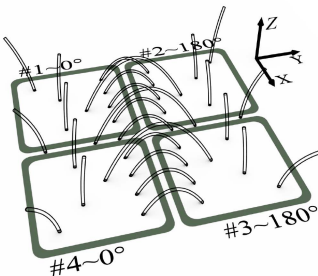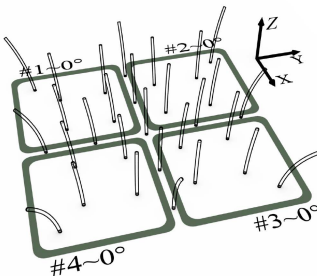VALIDATION OF x, y, AND z-DIRECTION MAGNETIC FIELD PROJECTIONS
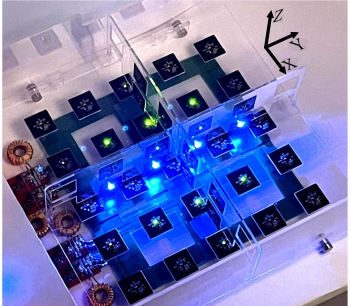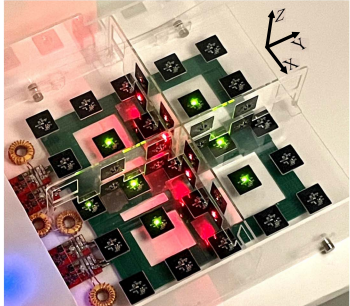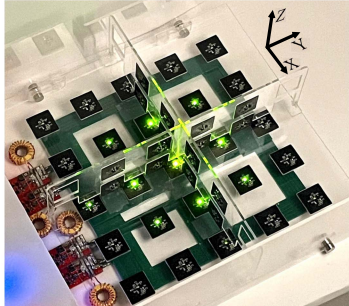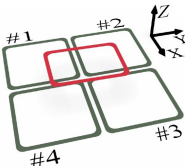
	x-direction Projection $(0°, 0°, 180°, 180°)$	y-direction Projection $(0°, 180°, 180°, 0°)$	z-direction Projection $(0°, 0°, 0°, 0°)$
Theoretical results			
Experimental results			

TABLE X
EXPERIMENTAL RESULTS OF SINGLE-RX DETECTION*

Scenes		x-direction Projection				y-direction Projection				z-direction Projection			
	# of Tx-coil	1	2	3	4	1	2	3	4	1	2	3	4
Experiment $\eta_{dc-dc} = 80.2\%$ $P_{out} = 51.8$ W	PA input current (A)	0.03	0.01	0.11	0.12	0.07	0.02	0.04	0.07	0.68	0.62	0.71	0.74
	Active (Y/N) $(I_{pa} > 0.28A)$	N	N	N	N	N	N	N	N	Y	Y	Y	Y
	Measured codeword	0	0	0	0	0	0	0	0	1	1	1	1
Theory	Calculated codeword	0	0	0	0	0	0	0	0	1	1	1	1
	Red-Rx codeword	0	0	0	0	0	0	0	0	1	1	1	1

* A nearly horizontal Red-Rx above Tx#1,2,3,4.

Both the cases with two Rxs and three Rxs have been investigated. Here, the results of the two-Rx detection are omitted to conserve space. Table XI lists the experimental results for the three-Rx detection. The three Rxs have different positions and orientations. As described in Section III-C, each Rx corresponds to a different set of four-bit binary codes in x, y, and z-direction magnetic field projections. These three sets of binary codes are superimposed together to form a final code representing the combined current positions and orientations of the three Rxs. This final code consistently matches the converted binary code derived from the actual measurements. Notably, the PA input dc currents in the y-direction projection are significantly higher compared to those in other directions. This indicates that there are more Rxs whose positions and orientations are relevant to the y-direction magnetic field projection.

D. Dynamic Rx Positions and Orientations

As show in Fig. 8, an experimental platform was built to verify, including a graphical user interface for real-time display of detection results and phase commands. First, the hardware system transmits real-time data to the host PC via Bluetooth.

TABLE XI
EXPERIMENTAL RESULTS OF THREE-RX DETECTION*

Scenes			x-direction Projection				y-direction Projection				z-direction Projection			
		# of Tx-coil	1	2	3	4	1	2	3	4	1	2	3	4
		PA input current (A)	0.78	0.26	0.03	0.16	0.70	1.08	0.90	0.38	0.55	0.93	0.56	0.03
Experiment	$\eta_{\mathrm{dc-dc}} = 77.6\%$ $P_{\mathrm{out,red}} = 13.6$ W $P_{\mathrm{out,yellow}} = 10.8$ W $P_{\mathrm{out,blue}} = 28.2$ W	Active (Y/N) ($I_{\mathrm{pa}} > 0.28$A)	Y	N	N	N	Y	Y	Y	Y	Y	Y	Y	N
		Measured codeword	1	0	0	0	1	1	1	1	1	1	1	0
Theory		Calculated codeword	1	0	0	0	1	1	1	1	1	1	1	0
		Red-Rx codeword	0	0	0	0	0	0	1	1	0	0	0	0
		Yellow-Rx codeword	1	0	0	0	1	0	0	0	1	0	0	0
		Blue-Rx codeword	0	0	0	0	0	1	1	0	0	1	1	0

* A nearly vertical Red-Rx above Tx#3,4, a Yellow-Rx above Tx#1, and a nearly horizontal Blue-Rx above Tx#2,3.

Then, the PC displays the Rx positions and orientations, Tx-coil output current phase commands, and Tx-coil dc input currents, updating every 0.5 s. The subfigures in Fig. 8 are the selected screenshots from a video. The timestamps of the screenshots are displayed in the lower-left corners of the screen. The recording was made using an iPhone 12, operating at a frame rate of 30 frames per second (fps). Note that the actual response time of the overall closed-loop system is 25 ms, as detailed in the following subsection. Due to the relatively slow Bluetooth data refresh rate, i.e., 0.5 s, there is a waiting time to display updated real-time data on the PC screen. All detection results in Fig. 8 are consistent with the actual Rx positions and orientations. For example, in the first subfigure, an Rx coil positioned over Tx#1 is accurately detected. The corresponding phase commands are $0°$, $180°$, $180°$, and $180°$, with Tx-coil dc input currents at 0.86 A, 0.14 A, 0.12 A, and 0.10 A.

Furthermore, Fig. 8 shows a continuous closed-loop-based detection and control process involving various Rx numbers, positions, and orientations.

1) Initially, a red Rx is positioned above Tx#1. Subsequently, this Rx moves to the center of the Tx-coil array, altering its orientation from horizontal to vertical. The MCU determines the current Rx position and orientation based on the four-channel Tx-coil dc input currents, and calculates corresponding phase-shift control signals within 25 ms. The transferred Rx dc output power reaches up to 40.2 W when the red Rx coil is vertical at time 0:41.
2) A yellow Rx is introduced, with both Rxs continually changing their positions and orientations. As shown in the 4th to 6th subfigures, the two Rxs receive respective amounts of dc output power under the closed-loop-based detection and phase-shift control. The average of the total dc output power in the 4th to 6th subfigures is 38.9 W.
3) Finally, the number of Rxs is increased to three. Again, the Tx-coil array simultaneously powers each Rx in a different position and orientation. The total Rx dc output power attains 45.7 W in the last subfigure.

E. Visualization of Detection and Control Process

Fig. 9 displays a complete closed-loop-based detection and control process as captured by a high-speed camera (Photron SA3 with 1000 fps, i.e., 1 ms time resolution). Here, each Rx coil is equipped with four LED sensors, emitting light of a color similar to its corresponding coil.

1) x-direction Projection (2955–2963 ms): The blue vertical Rx in x-direction and the z-direction yellow horizontal Rx on the edge are activated. Because no magnetic flux goes through the red Rx, the red LEDs of the red vertical Rx in y-direction are all OFF.
2) y-direction Projection (2963–2971 ms): Similarly, the red vertical Rx in y-direction and the z-direction yellow horizontal Rx on the edge are activated.
3) z-direction Projection (2971–2979 ms): As expected, only the LEDs in the z-direction yellow horizontal Rx are ON.
4) Detection and control (2980 ms): The STM32 and FPGA perform the Rx P&O detection and phase-shift control.

Finally, the Tx-coil array generates an optimal magnetic field to power all three Rxs, as shown in Fig. 9(d). The total duration of the closed-loop-based detection and control process is 25 ms, specifically from 2955–2980 ms. In particular, there is no need for communication between the Tx array and Rxs. All the above results confirm the effectiveness and simplicity of the proposed detection and control scheme for 3-D magnetic field shaping.

VI. DISCUSSIONS ON PRACTICAL ASPECTS

This article proposes to maximize the use of a 2-D planar Tx coil array to not only transfer power, but also act as a sensing device to detect the Rx positions and orientations. This fundamental concept could effectively help minimize the complexity and cost of future commercial WPT systems in sensing and communication. Meanwhile, in addition to the above theoretical analysis, several practical aspects need to be addressed, particularly through combining with commercialized device-to-device communication technology. For instance
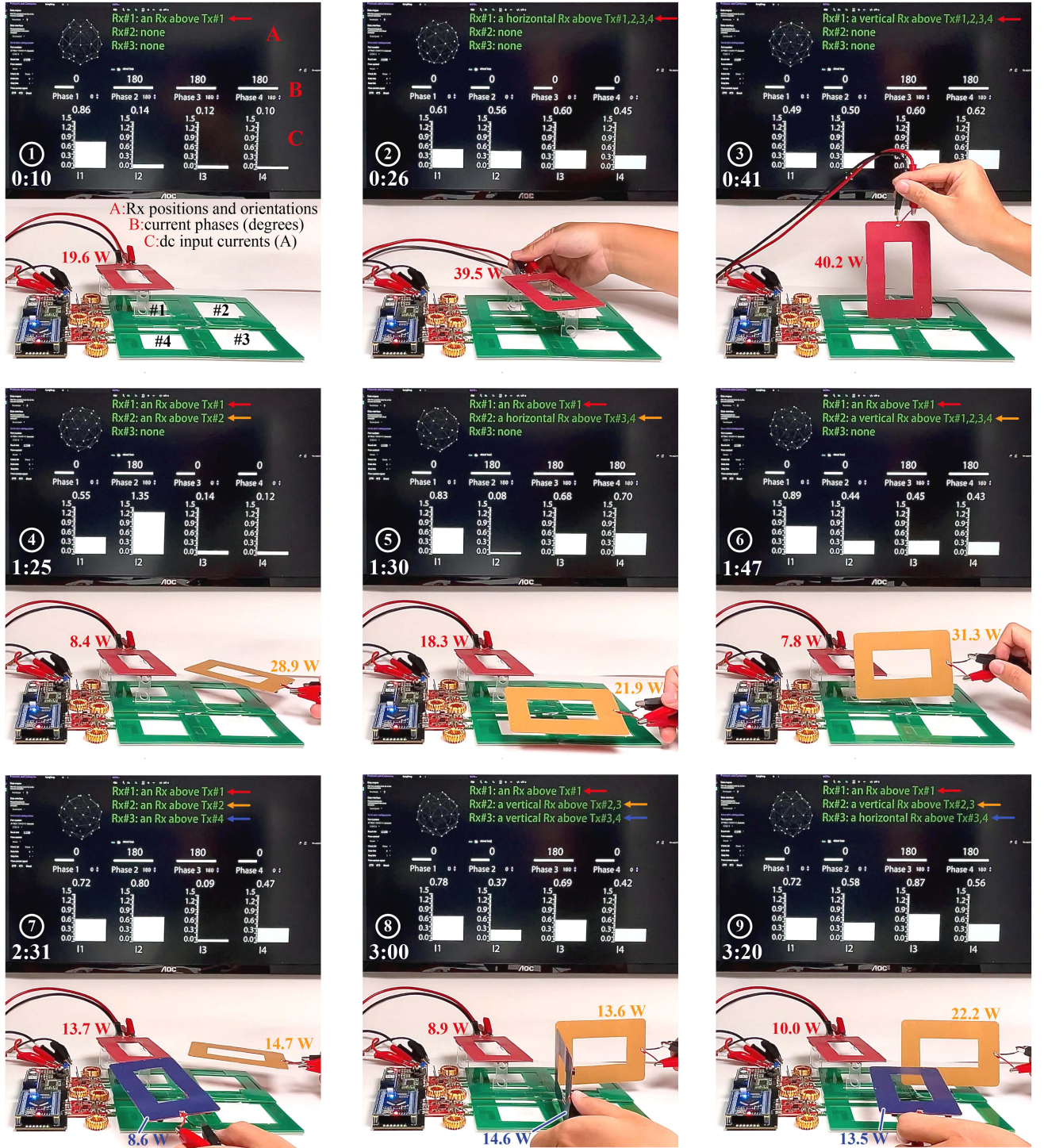
Fig. 8. Nine selected scenes of a continuous closed-loop-based detection and control process. For a full demonstration, refer to the video link: https://youtu.be/n5jzvEmgZy0 *FluxFlow - High-Freedom Wireless Charging*. Also, a smaller file version can be found in the multimedia supplementary materials included with this article.

1) *Foreign metallic object detection*: The proposed detection scheme can work with matured device-to-device communication such as Bluetooth. For instance, after the Rx position and orientation detection, if some supposed Rx device is unable to communicate, the presence of a foreign metallic object can be determined; while during operation, the entry of a foreign metallic object will cause a sudden drop in power transfer efficiency (i.e., additional power dissipation). The Tx-coil array can detect this entry by continuously monitoring power transfer efficiency and again screening through device-to-device communication. It is also possible to refer to and combine with existing foreign

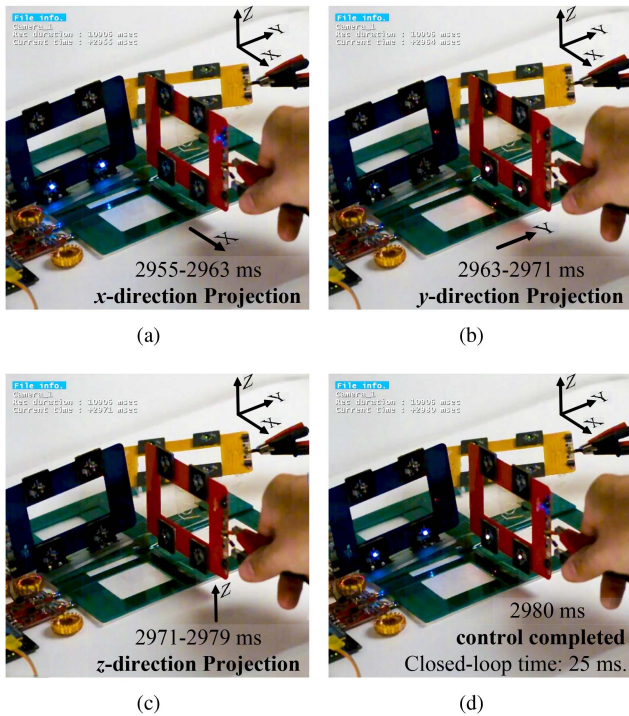Fig. 9. Slow motions of the closed-loop-based detection and phase-shift control (1000 fps). (a) x-direction Projection. (b) y-direction Projection. (c) z-direction Projection. (d) Detection and control. For a full demonstration, refer to the video link: https://youtu.be/-An6sU33iBo *FluxFrame - High-Speed Control Visualized*. Also, a smaller file version can be found in the multimedia supplementary materials included with this article.

object detection solutions, which have been intensively discussed in the literature, to further improve detection accuracy.

2) *Battery state-of-charge (SoC) variation:* This variation will result in different load conditions and required charging power. In the above experiments, even though the three Rxs have different dc loads of 5, 10, and 20 Ω, their positions and directions are detected correctly. As discussed in Section III, Rx position and orientation detection is encoded in a binary manner, making the detection robust. Communicating the battery SoC information with battery charging and management circuitry would help further fine tune the threshold for detection purposes, including a multilevel threshold, as briefly explained at the end of Section III.

3) *Battery aging and degradation*: Similarly, this will change the load condition and desired charging power. The proposed Rx position and orientation detection is a robust operation. Again, information exchange with the battery charging and management circuitry would help tailor the proposed detection and control scheme for aging batteries.

4) *Scalability:* As shown in Fig. 1, when there is a larger Tx coil-array and more Rxs, the Rx positions and orientations still fall into the four categories defined in Table II. Therefore, the magnetic field projection and coding-based Rx position/orientation detection are still valid. Since the presence of a specific Rx only affects the coding and phase combination of the Tx coils in its neighborhood, the added

cost and complexity are expected to be not significant. Meanwhile, for future practical applications, an optimal design needs to be developed to optimize the dimension of a Tx-coil array and the size of the individual Tx coils.

VII. CONCLUSION

This article presents a new closed-loop-based scheme to detect multiple Rx positions / orientations and control the magnetic field distribution accordingly. Based on an idea similar to the orthogonal projection of visible light, the concept of magnetic field projection in x, y, and z directions is discussed for the purpose of Rx detection. A complete algorithm is then developed to implement the closed-loop-based detection and control scheme. Both theoretical and experimental results effectively validate the full functionality of the new closed-loop-based scheme for various combinations of Tx-coil output current phases. The proposed magnetic field projection and current phase control pave the way to further enhance the spatial freedom of today's WPT through extendable 2-D planar Tx-coil arrays.

REFERENCES

[1] S. Y. R. Hui, W. Zhong, and C. K. Lee, "A critical review of recent progress in mid-range wireless power transfer," *IEEE Trans. Power Electron.*, vol. 29, no. 9, pp. 4500–4511, Sep. 2013.

[2] Z. Zhang, H. Pang, A. Georgiadis, and C. Cecati, "Wireless power transfer-an overview," *IEEE Trans. Ind. Electron.*, vol. 66, no. 2, pp. 1044–1058, Feb. 2019.

[3] S. Li, W. Li, J. Deng, T. D. Nguyen, and C. C. Mi, "A double-sided LCC compensation network and its tuning method for wireless power transfer," *IEEE Trans. Veh. Technol.*, vol. 64, no. 6, pp. 2261–2273, Jun. 2014.

[4] H. Kim et al., "Coil design and measurements of automotive magnetic resonant wireless charging system for high-efficiency and low magnetic field leakage," *IEEE Trans. Microw. Theory Tech.*, vol. 64, no. 2, pp. 383–400, Feb. 2016.

[5] Y. Sun, H. Zhang, A. P. Hu, C.-S. Tang, and L.-J. Xiang, "The recognition and control of nonideal soft-switching frequency for wireless power transfer system based on waveform identification," *IEEE Trans. Power Electron.*, vol. 32, no. 8, pp. 6617–6627, Aug. 2016.

[6] Y. Chen et al., "A clamp circuit-based inductive power transfer system with reconfigurable rectifier tolerating extensive coupling variations," *IEEE Trans. Power Electron.*, vol. 39, no. 2, pp. 1942–1946, Feb. 2024.

[7] A. Kurs, A. Karalis, R. Moffatt, J. D. Joannopoulos, P. Fisher, and M. Soljačić, "Wireless power transfer via strongly coupled magnetic resonances," *Science*, vol. 317, no. 5834, pp. 83–86, Jul. 2007.

[8] A. Pacini, A. Costanzo, S. Aldhaher, and P. D. Mitcheson, "Load-and position-independent moving MHz WPT system based on GaN-distributed current sources," *IEEE Trans. Microw. Theory Tech.*, vol. 65, no. 12, pp. 5367–5376, Dec. 2017.

[9] M. Liu, H. Zhang, Y. Shao, J. Song, and C. Ma, "High-performance megahertz wireless power transfer: Topologies, modeling, and design," *IEEE Ind. Electron. Mag.*, vol. 15, no. 1, pp. 28–42, Mar. 2020.

[10] Y. Guan, Y. Xiao, Y. Cui, and D. Xu, "Analysis and optimal design of mid-range WPT system based on multiple repeaters," *IEEE Trans. Ind. Appl.*, vol. 58, no. 1, pp. 1092–1100, Jan./Feb. 2022.

[11] J. Kim, D.-H. Kim, and Y.-J. Park, "Analysis of capacitive impedance matching networks for simultaneous wireless power transfer to multiple devices," *IEEE Trans. Ind. Electron.*, vol. 62, no. 5, pp. 2807–2813, May 2015.

[12] J. Li, R. Qin, J. Sun, and D. Costinett, "Systematic design of a 100-W 6.78-MHz wireless charging station covering multiple devices and a large charging area," *IEEE Trans. Power Electron.*, vol. 37, no. 4, pp. 4877–4889, Apr. 2022.

[13] J. Choi, D. Tsukiyama, Y. Tsuruda, and J. M. R. Davila, "High-frequency, high-power resonant inverter with eGaN FET for wireless power transfer," *IEEE Trans. Power Electron.*, vol. 33, no. 3, pp. 1890–1896, Mar. 2018.

[14] N. Ha-Van and C. Seo, "Analytical and experimental investigations of omnidirectional wireless power transfer using a cubic transmitter," *IEEE Trans. Ind. Electron.*, vol. 65, no. 2, pp. 1358–1366, Feb. 2018.

[15] N. Ha-Van, Y. Liu, P. Jayathurathnage, C. R. Simovski, and S. A. Tretyakov, "Cylindrical transmitting coil for two-dimensional omnidirectional wireless power transfer," *IEEE Trans. Ind. Electron.*, vol. 69, no. 10, pp. 10045–10054, Oct. 2022.

[16] C. Park, S. Lee, G.-H. Cho, S.-Y. Choi, and C. T. Rim, "Two-dimensional inductive power transfer system for mobile robots using evenly displaced multiple pickups," *IEEE Trans. Ind. Appl.*, vol. 50, no. 1, pp. 558–565, Jan./Feb. 2014.

[17] Y. Gu, J. Wang, Z. Liang, Y. Wu, C. Cecati, and Z. Zhang, "Single-transmitter multiple-pickup wireless power transfer: Advantages, challenges, and corresponding technical solutions," *IEEE Ind. Electron. Mag.*, vol. 14, no. 4, pp. 123–135, Dec. 2020.

[18] B. H. Choi, E. S. Lee, Y. H. Sohn, G. C. Jang, and C. T. Rim, "Six degrees of freedom mobile inductive power transfer by crossed dipole Tx and Rx coils," *IEEE Trans. Power Electron.*, vol. 31, no. 4, pp. 3252–3272, Apr. 2015.

[19] E. S. Lee, Y. H. Sohn, B. G. Choi, S. H. Han, and C. T. Rim, "A modularized IPT with magnetic shielding for a wide-range ubiquitous Wi-power zone," *IEEE Trans. Power Electron.*, vol. 33, no. 11, pp. 9669–9690, Nov. 2018.

[20] J. H. Kim et al., "Plane-type receiving coil with minimum number of coils for omnidirectional wireless power transfer," *IEEE Trans. Power Electron.*, vol. 35, no. 6, pp. 6165–6174, Jun. 2020.

[21] E. S. Lee, J. S. Choi, H. S. Son, S. H. Han, and C. T. Rim, "Six degrees of freedom wide-range ubiquitous IPT for IoT by DQ magnetic field," *IEEE Trans. Power Electron.*, vol. 32, no. 11, pp. 8258–8276, Nov. 2017.

[22] T. Feng, Z. Zuo, Y. Sun, X. Dai, X. Wu, and L. Zhu, "A reticulated planar transmitter using a three-dimensional rotating magnetic field for free-positioning omnidirectional wireless power transfer," *IEEE Trans. Power Electron.*, vol. 37, no. 8, pp. 9999–10015, Aug. 2022.

[23] C. Zhang, D. Lin, and S. Hui, "Basic control principles of omnidirectional wireless power transfer," *IEEE Trans. Power Electron.*, vol. 31, no. 7, pp. 5215–5227, Jul. 2015.

[24] W. Tang, Q. Zhu, J. Yang, D. Song, M. Su, and R. Zou, "Simultaneous 3-D wireless power transfer to multiple moving devices with different power demands," *IEEE Trans. Power Electron.*, vol. 35, no. 5, pp. 4533–4546, May 2020.

[25] H. Dan et al., "An extremum seeking algorithm based on square wave for three-dimensional wireless power transfer system to achieve maximum power transmission," *IEEE Trans. Ind. Appl.*, vol. 58, no. 1, pp. 1279–1288, Jan./Feb. 2022.

[26] D. Lin, C. Zhang, and S. R. Hui, "Mathematic analysis of omnidirectional wireless power transfer-Part-II three-dimensional systems," *IEEE Trans. Power Electron.*, vol. 32, no. 1, pp. 613–624, Jan. 2016.

[27] Z. Liu, M. Su, Q. Zhu, Y. Chao, S. Zang, and A. P. Hu, "A dual-frequency three-dimensional WPT system with directional power transfer capability at two separately regulated outputs," *IEEE Trans. Emerg. Sel. Topics Power Electron.*, vol. 11, no. 3, pp. 2514–2524, Jun. 2023.

[28] J. Feng, Q. Li, and F. Lee, "Load detection and power flow control algorithm for an omnidirectional wireless power transfer system," *IEEE Trans. Ind. Electron.*, vol. 69, no. 2, pp. 1422–1431, Feb. 2021.

[29] S.-Y. Kim, N.-R. Kwon, S.-H. Ahn, and W.-S. Lee, "Three-dimensional wireless power transfer system using multiple orthogonal resonators for spatial freedom," *IEEE Trans. Antennas Propag.*, vol. 71, no. 5, pp. 4036–4044, May 2023.

[30] T. Feng, Y. Sun, Y. Feng, and X. Dai, "A tripolar plane-type transmitter for three-dimensional omnidirectional wireless power transfer," *IEEE Trans. Ind. Appl.*, vol. 58, no. 1, pp. 1254–1267, Jan./Feb. 2022.

[31] B. H. Waters, B. J. Mahoney, V. Ranganathan, and J. R. Smith, "Power delivery and leakage field control using an adaptive phased array wireless power system," *IEEE Trans. Power Electron.*, vol. 30, no. 11, pp. 6298–6309, Nov. 2015.

[32] N. Kang, Y. Shao, M. Liu, and C. Ma, "Analysis and implementation of 3D magnetic field shaping via a 2D planar transmitting coil array," *IEEE Trans. Power Electron.*, vol. 37, no. 1, pp. 1172–1184, Jan. 2021.

[33] X. Li, B. Sun, J. Xu, S. Pang, and H. Li, "Design and analysis of misalignment insensitive wireless power transfer system based on multitransmitter for constant power," *IEEE J. Emerg. Sel. Topics Power Electron.*, vol. 11, no. 4, pp. 4536–4548, Aug. 2023.

[34] Y. Lim and J. Park, "A novel phase-control-based energy beamforming techniques in nonradiative wireless power transfer," *IEEE Trans. Power Electron.*, vol. 30, no. 11, pp. 6274–6287, Nov. 2015.

[35] Q. Zhu, M. Su, Y. Sun, W. Tang, and A. P. Hu, "Field orientation based on current amplitude and phase angle control for wireless power transfer," *IEEE Trans. Ind. Electron.*, vol. 65, no. 6, pp. 4758–4770, Jun. 2018.

[36] Y. Shao, H. Zhang, M. Liu, and C. Ma, "Explicit design of impedance matching networks for robust MHz WPT systems with different features," *IEEE Trans. Power Electron.*, vol. 37, no. 9, pp. 11382–11393, Sep. 2022.

Ning Kang (Member, IEEE) received the B.S. degree in information engineering with national scholarship honors from the Nanjing University of Aeronautics and Astronautics, Nanjing, China, in 2017, and the Ph.D. degree in electrical and computer engineering from the University of Michigan-Shanghai Jiao Tong University Joint Institute, Shanghai Jiao Tong University, Shanghai, China, in 2022.

He is currently a Research Fellow with the NTU Motor Lab, Nanyang Technological University, Singapore. His work centers on design and control strategies for megahertz wireless power transfer systems, high-speed control for MIMO systems, motor drives, and power converters.

Haojun Qin (Graduate Student Member, IEEE) received the B.S. degree in automation from Wuhan University, Wuhan, China, in 2020. He is currently working toward the Ph.D. degree in electrical and computer engineering with the University of Michigan-Shanghai Jiao Tong University Joint Institute, Shanghai Jiao Tong University, Shanghai, China.

His research interests include multiport dc–dc converters and their control strategies, especially for energy routing purposes.

Ruihan Ma (Graduate Student Member, IEEE) received the B.S. degree in information engineering with national scholarship honors from the South China University of Technology, Guangzhou, China, in 2021. He is currently working toward the Ph.D. degree in electrical and computer engineering with the University of Michigan-Shanghai Jiao Tong University Joint Institute, Shanghai Jiao Tong University, Shanghai, China.

His research interests include design and control strategies of kilohertz wireless power transfer systems, such as systems with multiple transmitters and receivers.

Christopher H. T. Lee (Senior Member, IEEE) received the B.Eng. (first class honors) and Ph.D. degrees in electrical engineering from the Department of Electrical and Electronic Engineering, The University of Hong Kong, Hong Kong, in 2009 and 2016, respectively.

He is currently an Associate Professor with Nanyang Technological University, Singapore. He was a Postdoctoral Fellow and a Visiting Assistant Professor with the Massachusetts Institute of Technology, Cambridge, MA, USA. He has authored or coauthored two books, four books chapters, and more than 230 referred papers. His research interests include electric machines and drives, renewable energies, and electromechanical propulsion technologies.

Dr. Lee was a recipient of the Croucher Foundation Fellowship in 2016, Li Ka Shing Prize (the best Ph.D. thesis prize) in 2017, Nanyang Assistant Professorship in 2019, NRF Fellowship in 2020, MDPI Energies Young Investigator Award and five Best Paper Awards, including First Place Best Paper Award in IEEE TRANSACTIONS ON ENERGY CONVERSION in 2022, JSPS Fellowship and IAS Myron Zucker Student-Faculty Grant in 2023, and the 10th Nagamori Award in 2024. He is an Associate Editor for IEEE TRANSACTIONS ON INDUSTRIAL ELECTRONICS, IEEE TRANSACTIONS ON ENERGY CONVERSION, *IEEE Access*, and *IET Renewable Power Generation*. He is the Chair of IEEE Vehicular Technology Society Singapore Section Chapter in 2023–2025. He is a Chartered Engineer in Hong Kong.

Ming Liu (Senior Member, IEEE) received the B.S. degree in mechatronic engineering from Sichuan University, Sichuan, China, in 2007, and the Ph.D. degree in electrical and computer engineering from the University of Michigan-Shanghai Jiao Tong University Joint Institute, Shanghai Jiao Tong University, Shanghai, China, in 2017.

From 2017 to 2020, he was a Postdoctoral Research Fellow with the Department of Electrical Engineering, Princeton University, Princeton, NJ, USA. He joined the School of Electronic Information and Electrical Engineering, Shanghai Jiao Tong University, Shanghai, China, in 2020, where he is currently an Associate Professor of electrical engineering. His research interests include megahertz wireless power transfer, battery management systems, and high frequency high performance power electronics for emerging applications.

Dr. Liu was the recipient of Top Ten Academic Star Award and Excellent Ph.D. Thesis Award Nomination from Shanghai Jiao Tong University in 2016 and 2018, Research Excellence Award from AirFuel Alliance, USA, in 2019, and Best Paper Award of IEEE ECCE-Asia in 2020. He was a Guest Editor for IEEE TRANSACTIONS ON INDUSTRIAL INFORMATICS and serves as Chair of the Wireless Power Transfer for Energy Storage Charging Subcommittee of Energy Storage Technical Committee, IEEE Industrial Electronics Society.

Chengbin Ma (Senior Member, IEEE) received the B.S. degree in industrial automation from the East China University of Science and Technology, Shanghai, China, in 1997, and the M.S. and Ph.D. degrees in electrical engineering from The University of Tokyo, Tokyo, Japan, in 2001 and 2004, respectively.

From 2004 to 2006, he was an R&D Researcher with the Servo Motor Laboratory, FANUC Limited, Yamanashi, Japan. From 2006 to 2008, he was a Postdoctoral Researcher with the Department of Mechanical and Aeronautical Engineering, University of California, Davis, USA. In 2008, he joined the University of Michigan-Shanghai Jiao Tong University Joint Institute, Shanghai Jiao Tong University, Shanghai, where he is currently a Professor of electrical and computer engineering. His research interests include battery and energy management, wireless power transfer, dynamics and motion control, and wide applications in electronic devices, electric vehicles, microgrids, smart grids, etc.

Dr. Ma was the recipient of many teaching and research awards at Shanghai Jiao Tong University, such as Koguan Top Ten Best Teacher Award in 2017 and Koguan Top Ten Research Group Award in 2014, and the recipient of Research Excellence Award from AirFuel Alliance, USA, in 2019. He is an Associated Editor for IEEE TRANSACTIONS ON INDUSTRIAL INFORMATICS (2016–2022) and *IEEE Journal of Emerging and Selected Topics in Industrial Electronics*. He served as Delegate of Energy Cluster (2019–2020), and is currently Delegate of Cross-disciplinary Cluster (2024–2025), IEEE Industrial Electronics Society.